Optical studies of the metal-nonmetal transition in a metal–rare-gas disordered system

O. Cheshnovsky, U. Even, and Joshua Jortner
Department of Chemistry, Tel-Aviv University, Tel Aviv, Israel
(Received 5 December 1980; revised manuscript received 20 July 1981)

In this paper we report the results of an experimental study of the optical properties in the energy range 0.65–3.80 eV of binary mixtures of Hg and Xe at 6 K over the concentration range $X = 1.0$–0.47 atomic fraction Hg. A new optical criterion for the specification of the metal-nonmetal transition (MNMT) is advanced which predicts that the real part of the low-frequency dielectric function should decrease abruptly with increase of the metal concentration beyond the MNMT. This prediction is borne out for the Hg-Xe system and was used to specify the concentration $X_M = 0.80 \pm 0.02$ for the MNMT. Subsequently, we have analyzed the frequency-dependent conductivity of the Hg-Xe films in terms of the random-phase model, which was extended to handle a system with two overlapping bands. The theoretical results were used to fit simultaneously the dc conductivity and the optical properties with a model density of states in the concentration range $0.47 \geq X \geq 0.88$. The marked overestimate of the dc conductivity calculated from the fit of the random-phase model for mercury concentrations $X < 0.80$ was interpreted in terms of the termination of the strong-scattering metallic regime where the states at the Fermi energy become localized. The composition $X_M = 0.80 \pm 0.02$, making the MNMT obtained from the onset of localization, is in excellent agreement with the independent estimate based on an optical criterion and with the onset of a positive temperature coefficient of the dc conductivity. Our analysis provides an unambiguous identification of the MNMT in this disordered material and draws a distinction between the MNMT ($X_M = 0.80 \pm 0.02$) and the conductivity onset ($X_C = 0.69 \pm 0.01$) in these low-temperature binary mixtures. We propose that the topological percolation threshold marks the conductivity transition and that in the composition range $X_C \leq X \leq X_M$ thermally activated hopping prevails, while a Mott-Anderson MNMT is exhibited at $X = X_M$.

I. INTRODUCTION

Experimental studies[1–16] of metal–rare-gas solid mixtures (MRGSM) have provided useful information regarding the metal-nonmetal transition[17] (MNMT) in compositionally and positionally disordered materials. Electronic structure and transport in MRGSM's were interrogated by various physical methods. The main effort was directed towards studies of the change of the electrical conductivity with concentration.[1–12] Also, optical properties,[4,6,7,9,13–15] the Mössbauer effect,[5] microscopic structure[16] and superconductivity[3,12] of those mixtures over a wide concentration range have been investigated. The variation of the electrical conductivity, σ, induced by changes of the metal atomic fraction, X, in MRGSM's falls into two categories:

(1) Abrupt conductivity transition marked by an abrupt drop of σ at a certain value of X, where $d\sigma/dX$ is discontinuous. No conclusive experimental evidence for such abrupt transition in disordered materials is available. The abrupt change of σ at a certain value of X reported for Cu-Ar (Ref. 2) and for Pb-Ar (Ref. 3) MRGSM's may originate from spurious crystallization effects.

(2) Continuous conductivity transition, which is characterized by a gradual decrease of σ with decreasing X. Such a behavior was observed for a variety of systems, e.g., Na-Ar,[11] Cs-Xe,[4] Rb-Kr,[4] Hg-Xe,[10] and Fe-Xe,[5] being exhibited at $X = 0.2$–0.6 for monovalent metals and at $X = 0.4$–0.8 for polyvalent metals.

We have been careful to use the term "conductivity transition" rather than MNMT. The onset of the conductivity in MRGSM's cannot be identified in general with the MNMT, as contributions from thermally activated hopping cannot be disregarded even at low temperatures. To provide a meaningful interpretation of the conductivity transition and to relate the conductivity transition to the MNMT it is imperative to have some information or to make some intelligent guesses regarding the microscopic structure of these materials. Two general classes of disordered two-component materials can be distinguished:

(a) Microscopically inhomogeneous MRGSM's consisting of metallic and insulating regions. Here two conditions have to be satisfied. First, the size of the metallic regions has to be sufficiently large so that the level spacing of the highly filled states is small relative to the thermal energy[18] and the parti-

cles are locally metallic. Second, the correlation length for the metallic regions has to be large relative to the mean free path (or the coherence length) of the conduction electrons in such metallic regions. With these conditions satisfied, the material has the characteristics of a granular metal. The electronic structure and transport in such inhomogenous materials can be handled in terms of classical percolation theory.[19–24]

(b) Microscopically homogeneous MRGSM: In such randomly substituted material, only statistical clustering of the metal atoms exists. In such homogeneous material an abrupt conductivity transition or a continuous conductivity transition can be exhibited.

Two central questions should be raised in relation to the electronic structure and transport in MRGSM's. First, is the structure of these materials microscopically inhomogeneous or homogeneous? In the former case, these materials can be considered as granular metals, which are reasonably well understood,[25] while, in the latter case, the nature of the MNMT requires further elucidation. Second, provided that the material is microscopically homogeneous, what is the proper description of the continuous MNMT? Two distinct physical pictures have recently been advanced for the description of the continuous MNMT in microscopically homogeneous MRGSM's. We have studied[10] the conductivity transition in the Hg-Xe MRGSM, where the MNMT essentially originates from band-overlap effects.[17] We have proposed[10] that this material is microscopically homogeneous and that the continuous conductivity transition should be interpreted in terms of the Mott-Anderson transition[17] intermediated by low-temperature thermally-activated hopping between large-radius localized states. A different point of view was advanced by Phelps, Avci, and Flynn,[4,7] who proposed that the conductivity onset in (microscopically homogeneous) MRGSM's can be adequately described in terms of an onset for classical percolation. This proposal is incompatible with our observation of activated conductivity in Hg-Xe in the vicinity of the conductivity transition.[10] It is still an open question whether the existence of an infinite connected structure of neighboring metal atoms in a well-dispersed MRGSM provides a sufficient condition for metallic conductivity to prevail in such disordered material.

In this paper we present the results of an experimental study of the optical properties of the Hg-Xe system, which provides a typical example for a microscopically homogeneous MRGSM. We shall demonstrate the implications of the information stemming from the optical properties of this disordered material for the following:

(A) Specification of the electronic structure over a broad concentration range.

(B) Characterization of the MNMT.

(C) Gaining indirect evidence regarding the microscopic structure of these materials.

The optical data for the Hg-Xe system, which were already briefly reported by us,[14] will be confronted with the predictions of the two available descriptions of the MNMT in MRGSM, i.e., the percolation picture and the Mott-Anderson picture. We shall show that the optical data together with our previous dc conductivity measurements[10] for Hg-Xe cannot be interpreted in terms of the percolation model. Subsequently, we shall analyze the optical data for the metallic samples in terms of the strong-scattering picture. Strong-scattering transport properties were accounted for in terms of the random-phase model (RPM), which was extended to handle the situation of band overlap in two band systems. We shall demonstrate that the termination of the strong-scattering metallic regime, as manifested by the breakdown of the RPM at low frequencies marks the MNMT in this disordered material. The MNMT in the Hg-Xe MRGSM specifies the Mott-Anderson "transition"[17] from the strong-scattering metallic regime to the thermally activated hopping regime. This analysis yields a self-consistent picture for the transport properties in this disordered material and, in particular, it will provide a distinction between the conductivity transition and the MNMT in MRGSM's.

II. EXPERIMENTAL PROCEDURES

A. Sample preparation

The Hg-Xe samples were prepared and measured in an ultrahigh vacuum system shown in Fig. 1, where the partial pressure of the residual gases was $\sim 1 \times 10^{-10}$ Torr. Xe gas was admitted to the system through a leak valve, while Hg was introduced through a nozzle of an oven kept at 20–150 °C. The partial pressures of Xe and of Hg during deposition were maintained at $\sim 10^{-5}$ Torr and continuously monitored using a quadrupole mass spectrometer. The gaseous mixtures were condensed on a sapphire window mounted on a He flow cryostat at 6 K. The absolute condensation rate of pure Xe was calibrated by the measurements of the oscillations in the optical transmission of Xe. The large number of oscillations (about 25), which correspond to $d = 1.5 \times 10^5$ Å film thickness, prove the high quality of the film and the uniformity of its thickness under our film deposition methods. The condensation rate of Hg was determined by atomic absorption analysis of Hg deposited on a gold foil, which was mounted on the cold (6 °K) substrate. A detailed description of the apparatus and the experimental procedures was provided by one of us.[26] The metal concentrations are believed to contain no more than 5% systematic and 1% random fractional uncertainties.

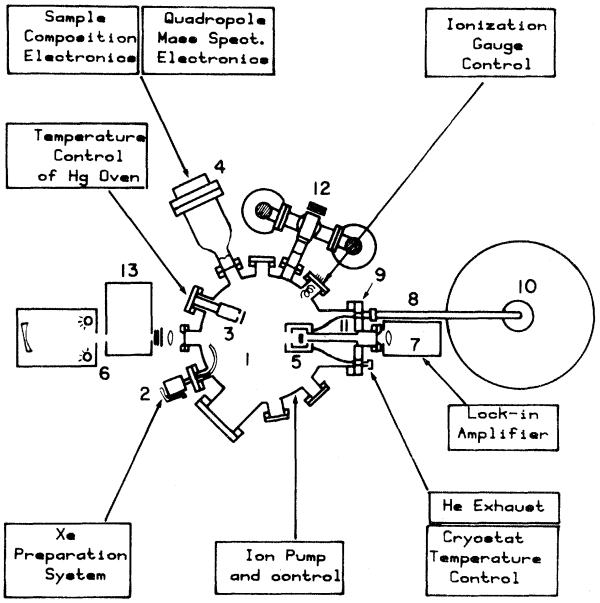

FIG. 1. Schematic representation of the experimental system: 1, ultrahigh vacuum vessel; 2, Xe leak valve; 3, Hg oven; 4, quadrupole mass spectrometer; 5, liquid-He flow cryostat; 6, light source; 7, optical detector; 8, transfer tube; 9, flange supporting the cryostat; 10, liquid-He container; 11, back baffle; 12, rough pumping system; 13, monochromator.

B. Optical measurements

Optical transmittance studies were performed in the energy range 0.65–3.80 eV (2000–326 nm), using a xenon lamp and quartz-halogen lamp as light sources. The light was dispersed at low resolution (5 Å) by a $\frac{1}{4}$-m Ebert monochromator (Model 82-410, Jarrell-Ash). At the exit slit of the monochromator the light was chopped with an optical scanner, then filtered with an appropriate optical filter, and finally focused through a window onto the sample on the substrate. The outcoming light was split to reach a silicon photodiode and a PbS detector. The ac signal of the detectors was fed into a lock-in amplifier (Model 9502, Brookdeal) and its analog output was recorded.

The transmittance data were experimentally determined as follows: The intensity, $I_s(\omega)$ of the light transmitted through the substrate at the photon frequencies ω was recorded. Then, deposition of a film with a known constant rate was initiated. Intensity measurements throughout the deposition were performed, monitoring the intensity $I_{fs}(\omega)$ transmitted through the film. The transmittance of the film on the substrate, $T_{fs}(\omega)$, is given by

$$T_{fs}(\omega)=\frac{I_{fs}(\omega)}{I_s(\omega)}T_s^{\rm calc}(\omega)\ , \tag{2.1}$$

where $T_s^{\rm calc}(\omega)$ is the calculated transmittance of the sapphire substrate according to the expression

$$T_s^{\rm calc}(\omega)=\frac{2n_s(\omega)}{1+n_s^2(\omega)}\ , \tag{2.2}$$

in which $n_s(\omega)$ is the refractive index of the sapphire substrate.[27] For each composition measurements were carried out for several values of film thickness d in the range $d=300$–5000 Å. The lowest film thickness utilized was $d\approx 300$ Å, to avoid systematic errors due to island structure and nonuniformity of the film, which should have been exhibited for lower d values.

The optical transmittance curves were analyzed using a classical-oscillator-fit method to extract the real part $\epsilon_1(\omega)$ and the imaginary part $\epsilon_2(\omega)$ of the dielectric constant. This method is based on the use of a simple analytical form for the dielectric function,[28] which consists of a sum of contributions from damped oscillators:

$$\epsilon(\omega)=\epsilon_1(\omega)+i\epsilon_2(\omega)=\epsilon_\infty+\sum_{i=1}^{N}\frac{s_i\omega_i^2}{\omega_i^2-\omega^2-i\Gamma_i\omega\omega_i}\ . \tag{2.3}$$

Here s_i, ω_i, and Γ_i are the strength, angular frequency, and width of the ith oscillator, respectively, ϵ_∞ is the contribution of high-frequency excitations to the dielectric function, and ω is the light angular frequency. This model dielectric function satisfies the Kramers-Kronig dispersion relation. It has been shown by Verleur[28] that a small number of oscillators is sufficient to describe a dielectric function that accounts for the experimental reflectance or transmittance curves over a wide energy range.

The fitting procedure involves an optimization process where the parameters of the oscillators are chosen, optical properties (e.g., reflectance or transmittance) are calculated and compared with the experimental results. This procedure is repeated to yield good correspondence between the calculated and the experimental data. We have characterized the dielectric function (2.3) in terms of four or five oscillators. The difference between the calculated and the measured values of the transmittance were minimized simultaneously for several films of different thickness and fixed composition using a general curve-fitting procedure.[29] At the end of the fitting procedure the relative difference between the calculated and the measured values of the transmittance was less than 5% over the entire energy range and for all film thicknesses. The transmittance, T, of the film situated on the nonabsorbing thick substrate

is given by

$$T = a[a_2\exp(4\pi kd/\lambda) + b_2\cos(4\pi nd/\lambda) + c_2\sin(4\pi nd/\lambda) + f_2\exp(-4\pi kd/\lambda)]^{-1} , \quad (2.4)$$

where the coefficients a, a_2, b_2, c_2, and f_2 are defined[30] in terms of the optical constants n_s, n, and k. Here, n_s is the real refractive index of the substrate, while n and k are the real and the imaginary parts of the refractive index of the film, respectively, which are related[31] to $\epsilon_1(\omega)$ and to $\epsilon_2(\omega)$.

C. Film thickness, density, and volume fraction

The film thickness d was evaluated from the experimental mass deposition rate and the estimated density of the samples. The density ρ of the mixed films was evaluated by assuming that the material consists of an amorphous alloy of hard spheres, characterized by the packing fraction $\eta = 0.45$.[32] The hard-sphere diameter of Xe was taken as $\sigma_{Xe} = 4.32$ Å.[33(a)] The hard-sphere diameter σ_{Hg} of Hg was taken from new experimental data[34] which reveal the dependence of σ_{Hg} on the density in expanded mercury. We invoked the assumption that σ_{Hg} in the Hg-Xe system depends on the effective mean density $\rho(\mathrm{Hg})$ in the two-component material in the same way as in the one-component expanded Hg. The density was determined from a graphical solution of the equation

$$\rho(\mathrm{Hg}) = Y\rho ,$$
$$\rho = \{(Y/\rho^*_{\mathrm{eff}}) + [(1-Y)/\rho_{Xe}]\}^{-1} , \quad (2.5)$$
$$\rho^*_{\mathrm{eff}} = K/\sigma^3_{Hg} ,$$

where Y is the mass fraction of Hg, and ρ_{Xe} is the density of pure amorphous xenon,[33(b)] being $\rho_{Xe} = 2.45$ g cm^{-3}, while ρ^*_{eff} is the effective density of a hypothetical sample of pure Hg which is composed of hard spheres with diameter σ_{Hg} being appropriate to the metal density $\sigma(\mathrm{Hg})$ in expanded mercury.[34] K is a constant chosen so that, according to this procedure, the density of pure Hg at $X = 1$ is $\rho(\mathrm{Hg}) = 13.7$ g cm^{-3}. Figure 2 describes the dependence of the density ρ and of the metal density $\rho(\mathrm{Hg})$ on the metal concentration X, as deduced from the solution of Eq. (2.5), using the σ_{Hg} data of Ref. 34.

For future discussion of the possibility that the Hg-Xe MRGSM consists of a dispersion of metallic grains in the solid rare gas, which will be presented in Secs. IV and VIII, we shall require an estimate of the metallic volume transition in a hypothetical microscopically inhomogeneous material. The volume

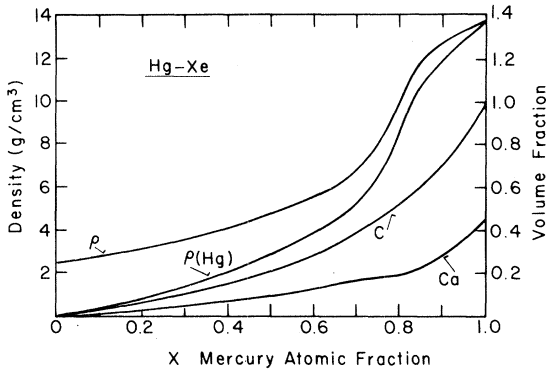

FIG. 2. Dependence of the density ρ, the Hg density $\rho(\mathrm{Hg})$, the volume fraction C, and the atomic volume fraction C_a, in the Hg-Xe system as a function of the Hg atomic fraction X.

fraction, C, of the metal in such a two-phase system can be estimated assuming that each of the constituents in the inhomogeneous two-component system retains its bulk properties. Accordingly, we take for the local densities the values $\rho_{Hg} = 13.7$ g cm^{-3} for (amorphous) Hg and $\rho_{Xe} = 2.45$ g cm^{-3} for (amorphous) xenon. Accordingly, the metallic volume fraction is

$$C = \frac{Y/13.7}{Y/13.7 + (1-Y)/2.45} . \quad (2.6)$$

Another pertinent quantity which will be required for the discussion of the transport properties and the MNMT is the volume fraction, C_a, of metal atoms in a microscopically homogeneous MRGSM. C_a is related to the metallic volume fraction C in the homogeneous material,

$$C_a = \eta\tilde{C}, \quad \tilde{C} = \rho(\mathrm{Hg})/\rho^*_{\mathrm{eff}} . \quad (2.7)$$

The composition dependence of C and C_a is presented in Fig. 2, together with the estimates of the densities of the films. This modification of the density scale, compared to our original evaluation of ρ,[10] modifies somewhat (by less than 50%) the absolute values of conductivity previously reported by us, while temperature coefficient of the conductivity remains unchanged. These modified conductivity data are displayed in Fig. 3. The composition $X_C = 0.69 \pm 0.04$, which marks the conductivity onset in the Hg-Xe systems determined by us, is higher than the recent observation of $X_C = 0.55 \pm 0.04$ reported by Goldman and colleagues[12] for this system. In view of the extreme care devoted by us to the absolute calibration of the metal concentration, we believe that the concentration scale presented herein is reliable.

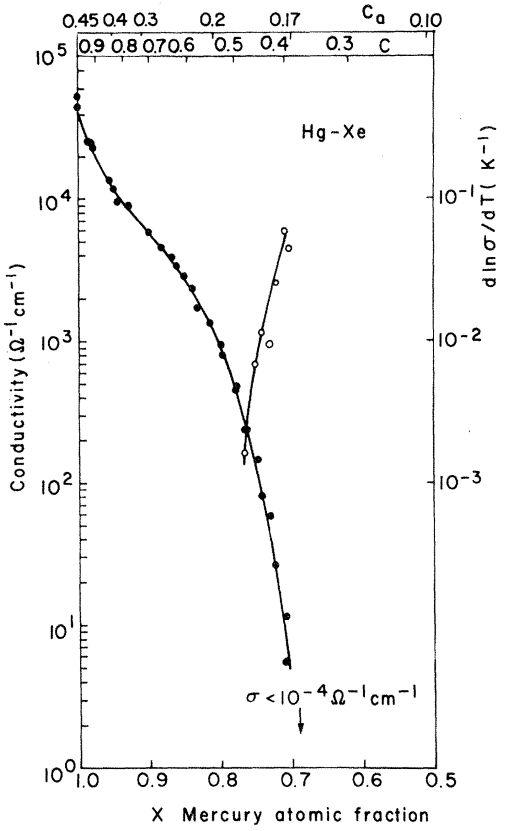

FIG. 3. Composition dependence of the conductivity (full circles) and of the temperature coefficient of the conductivity (TCC) (open circles) in Hg-Xe mixtures at 6 K. Three scales of mercury concentration are presented: X, the atomic fraction of Hg; C, the volume fraction of Hg; and C_a, the atomic volume fraction of Hg.

III. EXPERIMENTAL RESULTS

The optical constants were extracted from the experimental transmittance data for the following compositions of the Hg-Xe mixtures: $X=0.47$, 0.55, 0.66, 0.73, 0.77, 0.80, 0.83, 0.88, 0.96, and 1.00. A typical example of the transmittance data and the fitted transmittance for the extraction of the optical contants is displayed in Fig. 4. Figures 5 and 6 exhibit the real part of the dielectric constant $\epsilon_1(E)$ and the frequency-dependent conductivity $\sigma(E)=\epsilon_2(E)\omega/4\pi$ of Hg-Xe samples over the energy range 0.65–3.80 eV and over the metal composition range $X=1.0$–0.47. Here E(eV) is the energy and $\omega(\text{sec}^{-1})$ is the angular frequency. The dc conductivity $\sigma(0)$ for each alloy was plotted on the vertical axis of Fig. 6 and extrapolates quite smoothly to the optical data for $\sigma(E)$ at 0.65 eV. The optical data exhibit the following features:

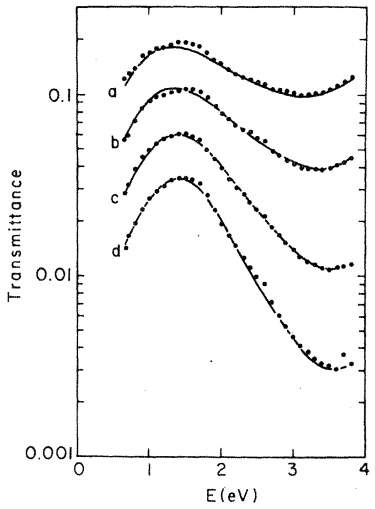

FIG. 4. Typical example for the fitting of a dielectric function consisting of classical oscillators (full line) to the experimental transmittance data of Hg-Xe mixtures (circles). The metal concentration is $X=0.96$. Curves a–d correspond to different values of the film thickness d.

(1) The optical conductivity of pure Hg deposited at 6 K shows a low-energy Drude-type tail and a broad maximum at 1.8 eV. These features are in qualitative agreement with the optical data of solid Hg,[35] the broad maximum at 1.8 eV being due to intraband transitions. The broadening and smearing of

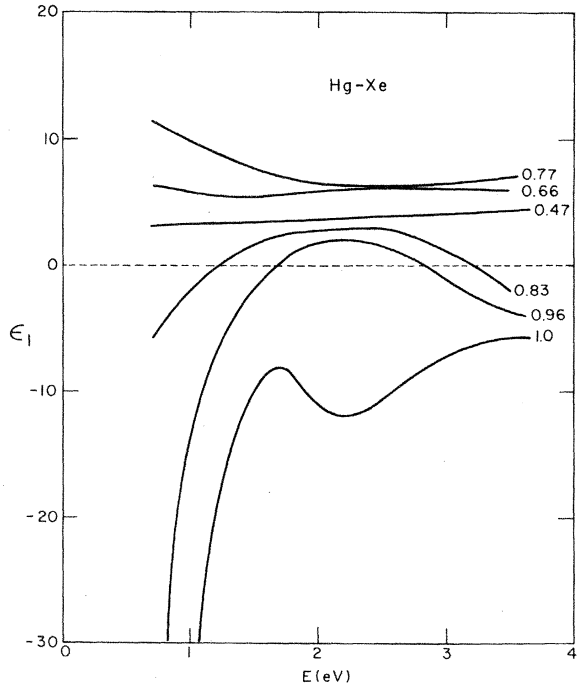

FIG. 5. Real part of dielectric function $\epsilon_1(E)$ for Hg-Xe mixtures at 6 K for different atomic fractions of mercury, X.

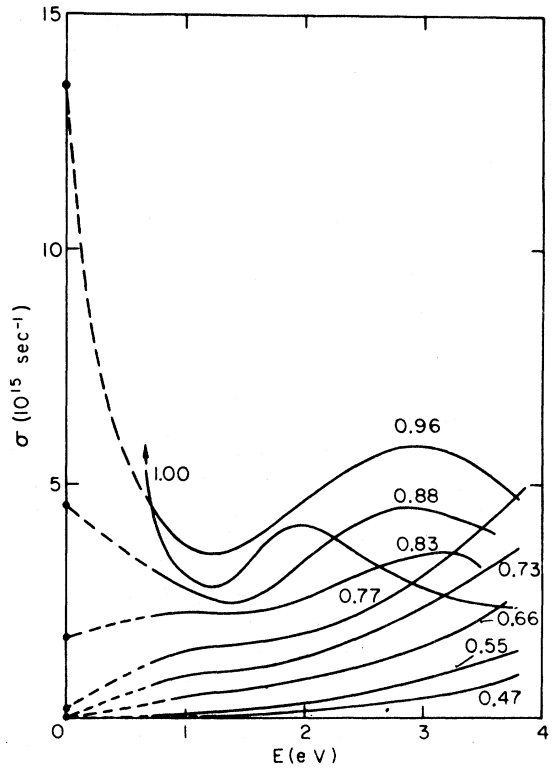

FIG. 6. Optical conductivity $\sigma(E)$ of Hg-Xe mixtures at 6 K for different atomic fractions of mercury. Solid line, experimental data from transmission measurements; broken line, extrapolation to the dc conductivity values, which are marked as dots.

the 1.8-eV peak in our samples relative to the 77 K crystal data originates from the partially disordered structure of pure Hg deposited at 6 K, which forms a polycrystalline material.[36] This conclusion concurs with our analysis[10] of the conductivity data of pure Hg.

(2) There is an appreciable difference between the optical data for pure mercury ($X=1$) and those for the $X=0.96$ films. The maximum at 1.8 eV for pure Hg moves to higher energies, peaking at 2.8 eV in the $X=0.96$ sample. At the same time the dc conductivity decreases from 4.5×10^4 $(\Omega\ \text{cm})^{-1}$ to 1.3×10^4 $(\Omega\ \text{cm})^{-1}$. The pure Hg films deposit in the form of a polycrystalline material.[36] On the other hand, the $X=0.96$ sample is presumably amorphous. The vanishing of the negative temperature coefficient of the dc conductivity provides support for this assertion. The difference between the properties of the polycrystalline and the amorphous material is strongly reflected by the appreciable change in the optical data in the narrow composition range $X=1-0.96$.

(3) For the compositions $X=0.88$ and $X=0.83$ the optical conductivity decreases at low energies, revealing a broad minimum about 1.2 eV, and subsequently starts rising, reaching a very broad maximum at 2.8 eV.

(4) In the narrow concentration range between $X=0.83$ and 0.77 a dramatic change in the characteristics of ϵ_1 are exhibited: ϵ_1 at low energies (0.65 eV) changes its sign from a negative value at high X to a positive value at the lower X value, as is apparent from Fig. 4.3. The change of the sign of ϵ_1 at low E is accompanied by a qualitative change of the slope of $\sigma(E)$ vs E curve in this energy range: the slope, which is negative at $X=0.88$, becomes positive at $X=0.77$.

(5) For $X<0.77$ the characteristics of $\epsilon_1(E)$ and of $\sigma(E)$ are those of an amorphous semiconductor, exhibiting, essentially, contributions to the dielectric function which originate from band-to-band transitions.

IV. IS THE Hg-Xe SYSTEM MICROSCOPICALLY INHOMOGENEOUS?

The electronic structure and transport as well as the nature of the MNMT in disordered materials are dominated by the microscopic structure of these systems. In the absence of structural data for the Hg-Xe system, one cannot rule out the possibility that the material is microscopically inhomogeneous, exhibiting the electronic structure, transport, and optical properties of a low-temperature granular metal. We have already pointed out[10] that the composition dependence of the conductivity and the temperature coefficient of the dc conductivity cannot be accounted for in terms of thermally activated tunnelling between metallic grains, providing evidence against the possibility that the Hg-Xe films have the structure of granular metals. We shall now provide additional evidence, which is based on the analysis of the optical data, demonstrating that the optical properties cannot be accounted for in terms of a structural model corresponding to a microscopically inhomogeneous material.

We proceed to examine the optical properties of a Hg-Xe two-phase mixture. A striking characteristic of the optical properties of small metallic particles dispersed in an insulator is the appearance of Mie resonance below the percolation threshold, as is the case for ganular metals.[37,38] At low C such a Mie resonance is expected to be exhibited at the energy E_{MI}, which satisfies the relationship $\epsilon_1^{\text{Hg}}(E_{MI})=-2\epsilon_1^{\text{Xe}}(E_{MI})$, where ϵ_1^{Hg} is the real part of the dielectric function for pure Hg, while $\epsilon_1^{\text{Xe}}=1.7$ is the square of the refractive index for amorphous Xe.[33(b)] Thus the Mie resonance is expected to occur at the energy where $\epsilon_1^{\text{Hg}}(E)=-3.4$. From the optical data for pure Hg obtained by Choke *et al.*,[35] we estimate the Mie resonance to be located at $E_{MI}=4.5$ eV.

This estimate of the position of the Mie resonance concurs with the experimental data for the optical properties of colloidal Hg particles.[39] In our work on the optical properties of insulating Hg-Xe films[15] we could not observe a Mie resonance in the nonmetallic region for $X=0.01-0.4$ up to energies of 5.5 eV. The estimate of E_{MI} presented above applies to low metal concentrations. At higher metal concentrations the position of the Mie resonance can be accounted for in terms of the Maxwell-Garnett theory (MGT),[40] which seems to be applicable for an inhomogeneous system consisting of grains of one material, e.g., metallic particles of type A embedded as isolated regions within a host matrix of another component of type B. We have shown that our experimental optical data are incompatible with the predictions of the MGT. This negative result—in particular, the absence of Mie resonances in the experimental data—indicates that the Hg-Xe system does not correspond to a dispersion of metallic grains in the rare-gas matrix.

An alternative description of the optical properties of an inhomogeneous material rests on the effective-medium theory (EMT), which treats the two components on an equal footing in terms of an effective-field theory. The dielectric function $\epsilon(\omega)=\epsilon_1(\omega)+i\epsilon_2(\omega)$ for the two-component system is obtained from the EMT equation[20–24]

$$C\frac{\epsilon^A(\omega)-\epsilon(\omega)}{\epsilon^A(\omega)+2\epsilon(\omega)}+(1-C)\frac{\epsilon^B(\omega)-\epsilon(\omega)}{\epsilon^B(\omega)+2\epsilon(\omega)}=0 \ . \tag{4.1}$$

It is convenient to write explicit solutions to Eq. (4.2) in the form

$$\epsilon(\omega)=\epsilon^A(\omega)f(C,X(\omega)) \ , \tag{4.2a}$$

$$f(C,X(\omega))=a(\omega)\pm\{[a(\omega)]^2+\tfrac{1}{2}X(\omega)\}^{1/2} \ , \tag{4.2b}$$

$$a(\omega)=\tfrac{1}{2}\{(\tfrac{3}{2}C-\tfrac{1}{2})[1-X(\omega)]+\tfrac{1}{2}X(\omega)\} \ , \tag{4.2c}$$

$$X(\omega)=\epsilon^A(\omega)/\epsilon^B(\omega) \ . \tag{4.2d}$$

The sign of the square root is chosen to give a solution with $\epsilon_2(\omega)=\mathrm{Im}\epsilon(\omega)\geq 0$.

We have used the EMT to calculate the optical properties of a microscopically inhomogeneous Hg-Xe system in the energies $E=0.65-3.8$ eV over the entire metal concentration range. It has been shown by Webman *et al.*[20–24] that a necessary condition for the validity of the EMT is $0.02\lesssim X(\omega)\lesssim 50$. This condition is satisfied for our system in the range of optical energies which we are interested in. The following input data were required for the EMT calculations C, $\epsilon_A(\omega)$, and $\epsilon_B(\omega)$. These were chosen in the following way:

(a) The C scale calculated using the bulk properties of the two components (see Fig. 2).

(b) The dielectric constant for Xe, which was specified by $\epsilon_1^{Xe}=1.7$ and $\epsilon_2^{Xe}=0$, with ϵ_1^{Xe} corresponding to the square of the refractive index of amorphous Xe.

(c) The dielectric function for Hg was chosen in three alternative ways: (c.1) Hg was characterized in terms of a Drude metal with a plasma energy $\hbar\omega_p=11$ eV and a relaxation rate $\hbar/\Gamma=1.5$ eV. (c.2) Our experimental optical data for pure Hg deposited at 6 K were taken to represent $\epsilon^A(\omega)$. (c.3) Our experimental data for the 95% Hg sample were taken to represent $\epsilon^A(\omega)$.

In Figs. 7 and 8 we present the results of EMT model calculations for the optical properties of the Hg-Xe system. The EMT calculation of $\sigma(E)$ for the Drude-metal–xenon system reveals no resemblance to the experimental data, indicating that this model is definitely too crude to describe the metallic regions. The situation is not improved by the use of the dielectric function for pure Hg [Fig. 7(b)], where in the EMT calculations the 1.8-eV peak of pure Hg survives over a broad concentration range down to $C\simeq 0.5$ ($X\sim 0.8$) in contrast with experimental $\sigma(E)$ data, which in the concentration range $0.76<X<0.95$ exhibit a broad peak at 2.8 eV. The use of the optical data of pure polycrystalline Hg for the EMT calculations of amorphous two-phase systems is questionable as one may argue that the metallic regions are amorphous. Therefore, we have also utilized the optical data of 95% Hg-Xe to represent $\epsilon^B(\omega)$ of the amorphous metallic regions (Fig. 8). Now the 2.8-eV peak in $\sigma(E)$ observed in the metallic regions is qualitatively reproduced by the EMT data. However, the following serious deviations between the results of the simulations [Fig. 8(b)] and the experimental data are exhibited. First, in the metallic region the heights of the 2.8-eV peaks of $\sigma(E)$ are considerably lower than predicted by the EMT [Fig. 8(b)]. Second, in the concentration range $0.70\leq X\leq 0.80$ ($C\simeq 0.5-0.4$), where the material is nonmetallic, the EMT results of Fig. 8(b) do not reproduce the experimental positive slope of $\sigma(E)$ vs E, but rather retain the metallic character. Third, the negative sign of ϵ_1 persists in the EMT calculations [Fig. 7(a)] over a broad range down to $C\cong 0.4$ ($X=0.7$), in contrast with the experimental data which exhibit a sign inversion at a higher metal concentration. The EMT predicts that in an inhomogeneous two-component system consisting of metallic and insulating regions the change of the electronic structure and the transport properties will be gradual, occurring over a broad concentration range. This expectation is not borne out by the experimental optical data, which cannot be accounted for in terms of the EMT. This failure of the EMT to account for the optical data supports the notion that the Hg-Xe films do not correspond to a two-phase MRGSM.

In addition, optical studies of Hg-Xe films in the

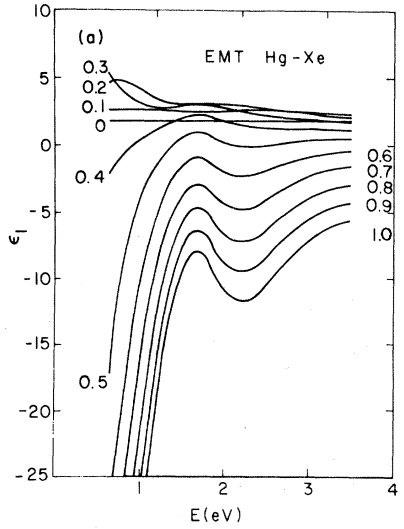

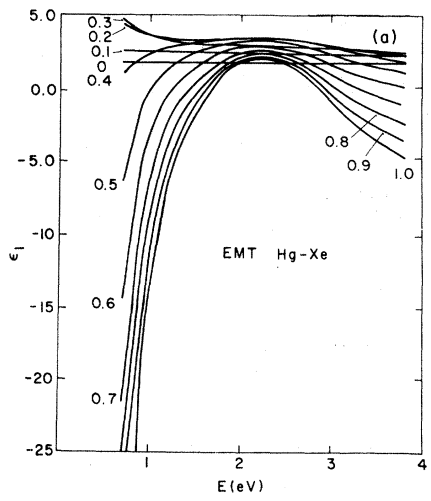

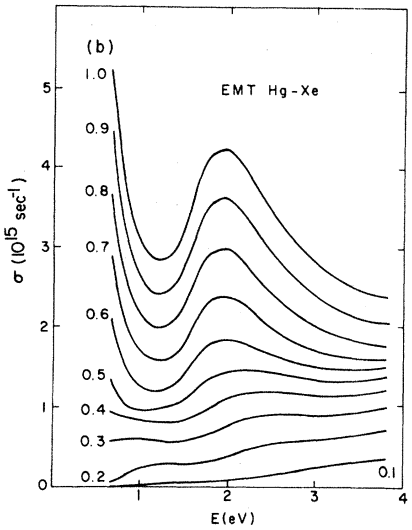

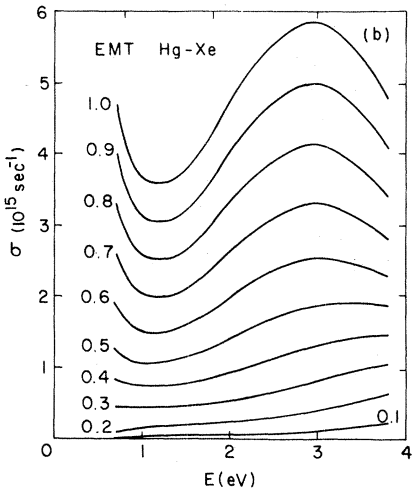

FIG. 7. (a) Real part of the dielectric function, $\epsilon_1(E)$, as calculated from the effective-medium theory for hypothetical Hg-Xe inhomogeneous mixtures. The metal clusters are characterized by the dielectric function extracted from our pure mercury data. Xenon is assumed to be amorphous with the real part of the dielectric function being 1.7 while the imaginary part equals zero. The numbers near each curve represent the volume fraction, C, of Hg. The appropriate atomic fraction of Hg can be obtained from Fig. 2. (b) Optical conductivity function $\sigma(E)$ as calculated from the effective-medium theory for hypothetical Hg-Xe inhomogeneous mixtures. The metal clusters are characterized by the dielectric function extracted from our mercury data. Xenon is assumed to be amorphous with the real part of the dielectric function being 1.7 while the imaginary part equals zero. The numbers near each curve represent the volume fraction, C, of Hg. The appropriate atomic fraction of Hg can be obtained from Fig. 2.

FIG. 8. (a) Real part of the dielectric function, $\epsilon_1(E)$, as calculated from the effective-medium theory for hypothetical Hg-Xe inhomogeneous mixtures. The metal clusters are characterized by the dielectric function extracted from our 95% mercury data. Xenon is assumed to be amorphous with the real part of the dielectric function being 1.7 while the imaginary part equals zero. The numbers near each curve represent the volume fraction, C, of Hg. The appropriate atomic fraction of Hg can be obtained from Fig. 2. (b) Optical conductivity function, $\sigma(E)$, as calculated from the effective-medium theory for hypothetical Hg-Xe inhomogeneous mixtures. The metal clusters are characterized by the dielectric function extracted from our 95% mercury data. Xenon is assumed to be amorphous with the real part of the dielectric function being 1.7 while the imaginary part equals zero. The numbers near each curve represent the volume fraction, C, of Hg. The appropriate atomic fraction of Hg can be obtained from Fig. 2.

concentration range $X=0.01-0.40$ (Ref. 15) reveal that the growth of the Hg monomer and the Hg dimer absorption bands obey the statistical rules for a random statistical distribution. This behavior drastically differs from the optical properties of granular metals, providing additional evidence against microscopic inhomogeneities in this material. We conclude that the Hg-Xe MRGM is microscopically homogeneous.

V. CHARACTERIZATION OF THE MNMT BY OPTICAL DATA

A central subject of the present work is the characterization of the MNMT in disordered materials by the optical data. The experimental data exhibit a simultaneous change in the behavior of $\epsilon_1(E)$ and of $\sigma(E)$ at low energies (0.65 eV) in the concentration range $X=0.83-0.77$, where ϵ_1 changes its sign from a negative to a positive value, while $\sigma(E)$ changes its slope from a negative to a positive value with decreasing X. This pattern of the low-energy optical data and, in particular, the abrupt change of ϵ_1 at low frequencies provides an optical criterion for the identification of the MNMT in the two-component system. The simultaneous change of the low-energy optical data can be rationalized in terms of the Kramers-Kronig dispersion relations,[41] which for our purpose can be presented in terms of an explicit expression for the real part of the dielectric function at a finite energy E ($E=\hbar\omega$),

$$\epsilon_1(E)=1+8P\int\frac{\sigma(y)\,dy}{y^2-\omega^2}$$

$$=1+8P\int\frac{[\sigma(y)-\sigma(0)]\,dy}{y^2-\omega^2}\ , \qquad (5.1)$$

where P stands for taking the principal value of the integral and $\sigma(y)=y\epsilon_2(y)/4\pi$ is the ac conductivity at the angular frequency y. We proceed to discuss the composition dependence of $\epsilon_1(E)$ at moderately low optical energies in the vicinity of the MNMT for microscopically homogeneous materials. In what follows we shall be concerned with the behavior of $\epsilon_1(E)$ at low but finite energies, so that the divergence of $\epsilon_1(E=0)$ originating from the polarization catastrophe at the MNMT[42,44] will be smoothed out.

Consider the MNMT induced by Anderson-Mott localization originating from band crossing or from the merging of Hubbard bands in a disordered material. We shall first discuss electronic structure and transport in the nonmetallic region below the MNMT. There is a range of energies bounded by the mobility edges E_C^- and E_C^+ below and above the Fermi energy E_F, respectively, in which all electronic states are localized. The energetic parameters

$$\xi^{\pm}=|E_C^{\pm}-E_F| \qquad (5.2)$$

are the characteristic energy spreads of the localized states. In the following discussion we shall assume that $\xi^+<\xi^-$, an extension to the other case being straightforward. The ac conductivity at $T=0$ is given by the Kubo-Greenwood formula

$$\sigma(y)=K\int_{E_F-\hbar y}^{E_F}dE\,|P_{IF}|^2N(E)N(E+\hbar y)/y \qquad (5.3)$$

with K being a numerical constant, $|P_{IF}|$ is the momentum operator between initial and final states and $N(E)$ is the density of states. The initial and final states can be localized or extended, i.e., bound or continuum states.

For bound-bound (BB) transitions between weakly localized states near the mobility edge the frequency-dependent conductivity obeys the ω^2 law[43]

$$\sigma_{BB}(y)=A\,\alpha^{-\eta}y^2\ , \qquad (5.4)$$

where A is a constant, the inverse localization length α is given by Mott and Davis[43] as $\alpha\propto\xi^{2/3}$, while $\eta=4-5$.[43] Accordingly, for BB transitions

$$\sigma_{BB}(y)=A\,\xi^{-2\eta}y^2,\quad \hbar y<\xi\ , \qquad (5.5)$$

where $\xi=\min(\xi^+ +\xi^-)$ and is the upper limit for the energy range where only BB transitions contribute to the conductivity.

For bound-continuum (BC) and continuum-continuum (CC) transitions the momentum operator elements will be taken to vary slowly with energy, so that

$$|P_{IF}|^2=D,\quad \hbar y>\xi\ . \qquad (5.6)$$

Thus at energies higher than ξ the contribution of BC transition to the optical conductivity will acquire the form

$$\sigma_{BC}(y)=KD\int_{E_F-\hbar y+\xi}^{E_F}dE\,N(E)N(E+\hbar y)/y\ , \qquad (5.7)$$
$$\hbar y>\xi\ .$$

As we are interested in the value of $\sigma(y)$ over a narrow energy range around ξ, we can assume the density of states to vary slowly with energy, so that

$$\sigma_{BC}(y)\equiv KD<N(E_F)N(E_F+\hbar y)>(\hbar y-\xi)/y$$
$$\hbar y>\xi\ . \qquad (5.8)$$

At energies higher than $\xi'=\max(\xi^+,\xi^-)$ an additional similar expression will account for continuum-bound transitions (CB). At energies higher than $\xi''=\xi^+ +\xi^-$ the BB transition will terminate while the CC transition sets in. When the energy spacing from the mobility edges decreases the character of the localized states approaches gradually that of the extended states. Thus, in the intermediate energy region

where BB, and BC transitions coexist Eqs. (5.5) and (5.8) will combine to yield a smooth optical conductivity function. The form of $\sigma(y)$ as a function of increasing metal concentration (i.e., decreasing ξ) is sketched in Fig. 9, where curve D denotes the highest concentration just above the MNMT concentration. Let us now consider a fixed energy E at which $\xi_1(E)$ is measured. We shall start with a system where $\xi > E$, as represented by curve A in Fig. 9. It is apparent from Eq. (5.1) that $\epsilon_1(E) \gtrsim 0$, as is expected in a nonmetallic system for energies within the mobility gap. Subsequently, we shall keep E fixed and decrease the range ξ of localized states, e.g., by increasing the metal concentration in a two-component system. When ξ approaches E from above (curve B, Fig. 9) the contribution to the integral in Eq. (5.1) increases as the positive contributions to the integral (at $\hbar y > E$) increase faster than the negative contributions (at $\hbar y < E$). Consequently, $\epsilon_1(E)$ will increase. This trend of increasing $\epsilon_1(E)$ with decreasing ξ is expected to continue when ξ crosses E, as described in curve C of Fig. 9. The further increase of $\xi_1(E)$ with decreasing ξ for $\xi \lesssim E$ can readily be understood by noting that $d\sigma(y)/dy$ decreases with decreasing y and the positive contributions to the integral in Eq. (5.1) dominates. A further decrease of ξ in the range $\xi < E$ may result in a decrease of $\xi_1(E)$. When this situation is reached, further decrease of ξ will result, in principle, in a monotonic decrease of $\xi_1(E)$ in the nonmetallic region. However, for the physical systems which are of interest to us the optical energy E can be chosen so that the density of states varies weakly with energy in the range $E_F - E$ to $E_F + E$, i.e.,

$$\frac{dN(E_F)}{dE}[N(E_F)]^{-1} . \tag{5.9}$$

We recall that the Mott-Anderson delocalization occurs with increasing metal concentration. In the energy range E_F to $E_F \pm E$, where the density of states is relatively flat, according to condition (5.7), a small increase in the metal concentration will result in the delocalization of electronic states over this entire region. We thus expect that ξ decreases fast with increasing X. Under these circumstances, the composition range in which $\epsilon_1(E)$ decreases with decreasing ξ in the nonmetallic region below the MNMT is expected to be very narrow. When the MNMT is reached, $\sigma(y)$ abruptly assumes a finite value of $\sigma_{\min}$, which corresponds to the minimum metallic conductivity over the range $\hbar y = 0$ to $\hbar y = E$ (Curve D, Fig. 9). Consequently, $\epsilon_1(E)$ will exhibit an abrupt decrease at the composition marking the MNMT. In real life, when $\epsilon_1(E)$ is investigated at the optical energy E, which is sufficiently low according to condition (5.7), it will exhibit a sharp decrease over a narrow composition range near the MNMT composition. Figure 9 portrays the general features of $\epsilon_1(E)$ in the vicinity of the MNMT, where $\epsilon_1(E)$ decreases fast at the composition marking the MNMT. Finally, we shall consider the characteristics of $\epsilon_1(E)$ in the metallic region at a sufficiently low optical energy located within the pseudogap. Now $\sigma(0)$ increases faster than $\sigma(y)$ at finite frequencies with the increase of the composition X. Consequently, according to Eq. (5.1), $\epsilon_1(E)$ is expected to decrease with increasing the metal composition in the metallic region.

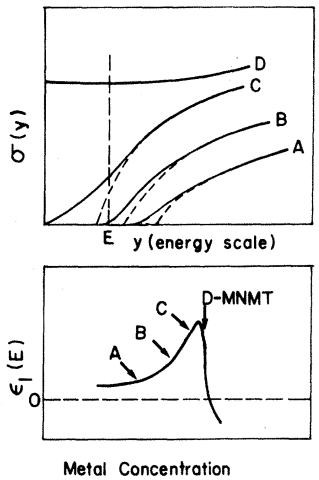

FIG. 9. Concentration dependence of the optical conductivity $\sigma(y)$ and the real part of the dielectric function $\epsilon_1(E)$ at a fixed low energy E, as an expanded metal approaches the MNMT due to Anderson delocalization. The letters A to D denote increasing metal concentration. The broken lines represent the contributions of the bound-continuum transitions to the optical conductivity.

The abrupt change of $\epsilon_1(E)$, at a relatively low optical energy E, at the MNMT constitutes an optical criterion for the identification of the onset of delocalization, in microscopically homogeneous materials. This optical criterion for the identification of the MNMT provides a practical extension of an exact criterion for the characterization of the MNMT in terms of a discontinuous change in the real part of the static dielectric constant $\epsilon_1(0)$. The characteristics of $\epsilon_1(0)$ in the vicinity of the MNMT are discussed elsewhere[44] and are related to the problem of the dielectric catastrophe.

We have analyzed the composition dependence of the $\epsilon_1(E)$ data at $E = 0.65$ eV in terms of the optical criterion for the identification of the MNMT in Hg-Xe films. The optical energy $E = 0.65$ eV, corresponding to the lowest energy studied by us is adequate for the application of the optical criterion as, on the basis of theoretical calculations of expanded Hg,[45] as well as according to the numerical simulations of the density of states reported in Sec. VII, we assert that the density of states in the vicinity of the Fermi energy for the composition range $X \geq 0.66$ varies

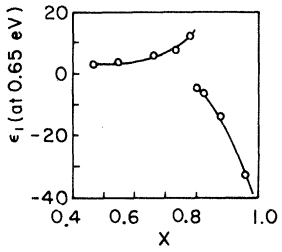

FIG. 10. Real part of the dielectric function, ϵ_1, at the energy 0.65 eV in Hg-Xe mixtures as a function of Hg concentration X.

weakly with energy over the energy range E_F to E_F+E, so that condition (5.7) is obeyed in accordance with the estimate of Mott.[46] In Fig. 10, we show the concentration dependence of $\epsilon_1(E)$ at $E=0.65$ eV, the lowest energy studied by us. In the concentration range $X<0.77$, $\epsilon_1(0.65\text{ eV})$ is positive and increases with increasing X, whereupon this composition range corresponds to the nonmetallic region, where localization occurred. In the concentration range $X>0.80$, $\epsilon_1(0.65\text{ eV})$ is negative and the material is metallic. In the concentration range $0.77\leq X\leq 0.80$, $\epsilon_1(0.65\text{ eV})$ exhibits a discontinuous change and we assert that the change of sign of this quantity at the composition $X_M=0.80\pm0.02$ marks the MNMT in the Hg-Xe system.

It is important to emphasize that the application of the optical criterion to the MNMT in Hg-Xe films yields a value of the metal concentration X_M, characterizing the MNMT that is distinct from the concentration X_C which marks the conductivity transition. The composition $X_C=0.69$ marks the conductivity transition, while in the range $X=0.69-0.77$, where the system is conducting at 6 K (see Fig. 3) the positive values of $\epsilon_1(0.65\text{ eV})$ and its X dependence clearly indicates that the system is nonmetallic. The identification of $X_M=0.80\pm0.02$ for the MNMT in Hg-Xe, on the basis of the optical criterion, is in excellent agreement with our analysis of the dc conductivity data for this system,[10] where the onset of the negative temperature coefficient of the conductivity sets in at $X=0.79$, a composition which we have identified as the onset of localization. It is gratifying that the dc conductivity and the optical data provide an unambiguous identification of localization in a disordered material which exhibits an apparently continuous MNMT.

VI. RANDOM-PHASE MODEL FOR A TWO-BAND SYSTEM

On the basis of the optical criterion for the MNMT, we assert that the Hg-Xe system is metallic at $X\geq 0.80$. In the composition range $0.88\geq X\geq 0.80$ the dc conductivity varies in the range $\sigma=3000-600\ (\Omega\text{ cm})^{-1}$. This conductivity range in the one-component expanded Hg was assigned to the strong-scattering transport regime. We propose that the composition range $0.80\leq X\leq 0.88$ in Hg-Xe corresponds to the strong-scattering, diffusive-metallic-transport regime. According to Cohen,[47] Mott,[48] Hindley,[49] and Friedman[50] the strong-scattering situation is not limited to metallic systems, being applicable to the general case of extended states in any strongly disordered systems. Thus, one can apply the strong-scattering picture for the dc conductivity and the optical properties of some metallic systems, where all electronic states are extended, as well as the optical properties of nonmetallic systems for the energies where the contribution from continuum-continuum transition dominates.

The strong-scattering model has been utilized previously in an attempt to account for the dc transport properties of metallic expanded Hg in the density range 11.0–9.0 g cm^{-3}.[51] We shall attempt to apply this model for the dc conductivity and optical properties in the metallic strong-scattering regime $X=0.88-0.80$, and for the optical properties over the nonmetallic composition region $X=0.80-0.47$ in Hg-Xe. However, the RPM as developed for a single s band is not directly applicable for the Hg-Xe system, where the effects of s-p–band overlap prevail. While the dc conductivity in the strong-scattering metallic regime can be analyzed, at least semiquantitatively, in terms of the single-band RPM, a coherent description of the optical properties requires an extension of the RPM to account for a two-band situation.

In what follows, we shall apply an extended version of the RPM to analyze the optical data over the composition range $X=0.88-0.45$, as well as the dc conductivity data in the metallic strong-scattering regime. There are two major goals for this analysis. Firstly, we shall demonstrate that the RPM is adequate to describe the high-frequency $E=0.65-3.8$ eV optical data over a broad composition range, which spans both the strong-scattering metallic regime as well as the nonmetallic regime, where the states in the pseudogap are localized. Secondly, we shall demonstrate that the analysis of the dc conductivity data in terms of the RPM combined with model density of states functions can be utilized to characterize the MNMT. We shall show that the termination of the strong-scattering metallic regime, which is manifested by the breakdown of the RPM at low frequencies, marks the MNMT in Hg-Xe. Our analysis will proceed in three stages: Firstly, we shall derive a generalization of the RPM for the frequency-dependent conductivity in a two-band system. We shall show that the transport properties within the RPM can be recast in terms of a convolution integral modified by an energy-

dependent transition moment, which accounts for the two-hand features of the problem. Secondly, in Sec. VII we shall advance semiempirical models for the density of states in the Hg-Xe system, which will be utilized for the analysis of the optical data. Thirdly, we shall examine the dc conductivity data demonstrating that the breakdown of the RPM at low frequencies marks the MNMT in this system.

In Appendix A we extend the RPM for a two-band system, considering explicitly the s and p bands in the Hg-Xe system. The frequency-dependent conductivity is given by

$$\sigma(\omega)=\frac{A}{\omega}\left[I\int_{E_F-\hbar\omega}^{E_F}dE\,[N_s(E)N_p(E+\hbar\omega)+N_p(E)N_s(E+\hbar\omega)-2N_{sp}(E)N_{sp}(E+\hbar\omega)]\right.$$
$$\left.+ZK\int_{E_F-\hbar\omega}^{E_F}dE\,[N(E)N(E+\hbar\omega)+2N(E)N_{sp}(E+\hbar\omega)+2N_{sp}(E)N(E+\hbar\omega)+4N_{sp}(E)N_{sp}(E+\hbar\omega)]\right], \tag{6.1}$$

where

$$A=\pi e^2\hbar N^{-1}\Omega/m^2=\pi e^2\hbar/m^2 n(\mathrm{Hg}) \ , \tag{6.1a}$$

with $n(\mathrm{Hg})$ being the number density of Hg. I is the one-center integral [Eq. (A8)]; K is the two-center integral [Eq. (A10)]; $N_s(E)$ and $N_p(E)$ denote the s and p densities of states, respectively [Eqs. (A13)]; $N_{sp}(E)$ corresponds to the hybrid density of states [Eq. (A16)]; and $N(E)$ is the total density of states [Eq. (A15)]. The RPM result for the frequency-dependent conductivity of a two-band system provides a generalization of the results of Hindley[49] and of Friedman.[50] The following features of the frequency-dependent conductivity should be noted:

(1) The optical conductivity for the two-band system is determined both by an intrasite one-center contribution and by intersite two-center contributions. This situation differs from the one-band case, in which only two-center contributions appear.

(2) The frequency-dependent conductivity [Eq. (A18)] can be expressed in terms of a convolution integral between the total densities of states modified by a transition operator

$$\sigma(\omega)=\frac{A}{\omega}\int_{E_F-\hbar\omega}^{E_F}dE\,M(E,\omega)N(E+\hbar\omega)N(E) \ , \tag{6.2}$$

$$M(E,\omega)=ZK[1+2\alpha(E+\hbar\omega)\beta(E+\hbar\omega)+2\alpha(E)\beta(E)+4\alpha(E)\beta(E)\alpha(E+\hbar\omega)\beta(E+\hbar\omega)]$$
$$+I[\alpha^2(E)\beta^2(E+\hbar\omega)+\alpha^2(E+\hbar\omega)\beta^2(E)-2\alpha(E)\beta(E)\alpha(E+\hbar\omega)\beta(E+\hbar\omega)] \ , \tag{6.2a}$$

where the coefficient A is given by Eq. (6.1a), Z is the coordination number, K is the two-center integral [Eq. (A10)], and $N(E)$ denotes the total density of states [Eq. (A14)], while $\alpha(E)$ and $\beta(E)$ are the expansion coefficients of s and p basis states at energy E. The energy dependence of the transition operator $M(E,\omega)$ [Eq. (6.2a)] accounts for the distinct contributions of the two bands. This energy dependence of $M(E,\omega)$ is distinct from the energy dependence of the transition operator in some amorphous semiconductors which are traced to band-structure effects smeared out by disorder.[52,53]

(3) The dc conductivity $\sigma(0)$ is obtained from Eq. (6.1) in the limit $\omega\to 0$. The contribution of the one-center intrastate terms vanishes and $\sigma(0)$ takes the form

$$\sigma(0)=AKZ\{[N(E_F)]^2+4N(E_F)N_{sp}(E_F)+4[N_{sp}(E_F)]^2\} \ , \tag{6.3}$$

where $N_{sp}(E)$ is the hybrid density of states [Eq. (A16)] at the Fermi energy. The vanishing of the one-center contribution in the low-frequency limit makes sense, as only charge displacement will contribute to the dc conductivity. Equation (6.3) reflects the effect of s and p populations at the Fermi energy E_F to the dc conductivity. Only when $\alpha(E_F)\sim\beta(E_F)$ do we expect that $\sigma(0)\propto[N(E_F)]^2$, regaining the well-known single-band result. This state of affairs may apply reasonably well to expanded Hg over the density range 11.0–9.0 g cm^{-3}, providing some justification to the application of the one-band result to the analysis of dc transport in that system.

(4) In the limit of very high frequencies the major contribution to $\sigma(\omega)$ originates from regions where the s-p overlap is negligible. Accordingly, we can set $N_s(E)=N(E)$, $N_p(E+\hbar\omega)=N(E+\hbar\omega)$, $N_s(E+\hbar\omega)=N_p(E)=0$, and $N_{sp}(E)=N_{sp}(E+\hbar\omega)=0$. Equation (6.1) then reduces to the simple form

$$\sigma(\omega)\cong\frac{A}{\omega}\int_{E_F-\hbar\omega}^{E_F}dE\,N(E)N(E+\hbar\omega)(I+ZK) \ , \tag{6.4}$$

regaining the conventional expression in this limit.

(5) The relative contributions from the intersite terms and the intrasite contributions to the optical conductivity can be estimated from the ratio, K/I, of the two-center and the one-center transition moments. The integrals I [Eq. (A8)] can be expressed in an approximate form in terms of the atomic properties of the Hg atom

$$I \cong E_{sp}^2 \langle X \rangle^2 m^2/h^2 \cong m E_{sp} f/2 \ , \tag{6.5}$$

where E_{sp} is the atomic excitation energy for the $^1S_0 \rightarrow {}^1P_1$ transition $\langle X \rangle^2$ corresponds to the X component of the transition for this transition, while f represents the oscillator strength for this transition. The K integral [Eq. (A10)] can be approximated in terms of the two-center exchange integral[54]

$$K \cong a^2 J^2 m^2/h^2 \ , \tag{6.6}$$

where a is the lattice spacing, while J is the exchange integral between nearest-neighbor Hg atoms. From Eqs. (6.3) and (6.6) we get

$$K/I = (2/f)(J/E_{sp}) a^2 J m/h^2 \cdot \ . \tag{6.7}$$

Taking $E_{sp} = 6.5$ eV, $f = 1$ from atomic data and $J = 0.5$–0.7 eV from model band-structure-model calculations for liquid Hg, we estimate $K/I \cong 0.1$, which is reliable within a numerical factor of 2. Note, that at high Hg concentrations Z is large and $ZK \sim I$ (with this estimate), so that the contribution from one-center and from the two-center terms are comparable. At low Hg concentration Z is small and $ZK \leq I$, so that the one-center contribution becomes dominant, as is expected.

VII. APPLICATION OF THE RANDOM-PHASE MODEL TO THE OPTICAL PROPERTIES

We have utilized the theoretical result, Eq. (6.1), for the frequency-dependent conductivity, together with the experimental optical transmittance data for Hg-Xe films to extract information concerning the density-of-states functions in Hg-Xe MRGSM's over the composition range $X = 0.88$–0.47. In the strong-scattering metallic regime we have used the optical data, together with the dc conductivity to provide a fit of $\sigma(\omega)$ from zero frequency up to $E = 3.8$ eV. These numerical simulations provide useful information regarding the electronic structure and the MNMT in Hg-Xe. We proceeded to fit the optical data by model density of states adopting the following general procedure:

(a) The density-of-states functions were specified: The densities of states $N_s(E)$ and $N_p(E)$ were taken to be characterized by the following three features. First, analytical functions whose energy dependence resembles the general features of density-of-states functions calculated for expanded Hg (Ref. 45) as well as that of randomly distributed donors.[55,56] Second, the hybrid density of states [Eq. (A16)] could be expressed by an analytic function. Third, the convolution integrals in Eq. (6.1) can be performed analytically.

Two forms for model densities of states were adopted: (a1) Gaussian (GA) bands,

$$N_s(E) = Z_1 \exp(-a_1 E^2) \ , \tag{7.1a}$$

$$N_p(E) = Z_2 \exp[-a_2 (E - C^2)] \ ; \tag{7.1b}$$

(a2) square difference of exponents (SQDE) densities of states,

$$N_s(E) = W_1 \{\exp[-b_1 (D - E)] - \exp[-b_1 r_1 (D - E)]\}^2 \ , \tag{7.2a}$$

$$N_p(E) = W_2 \{\exp[-b_2 (D + E)] - \exp[-b_2 r_2 (D + E)]\}^2 \ . \tag{7.2b}$$

The relative areas of the s and p bands were 1:3, as implied by the threefold degeneracy of the p band, while the relative widths of the s and p bands were about 1:1.5 following the model calculations of Yonezawa *et al.*[45] for expanded Hg. During the optimization process of the highest Hg concentration $X = 0.88$, the area of the s band was treated as an adjustable parameter. Subsequently, for lower concentrations the area of the s band was scaled (relatively to the area at $X = 0.88$) to be proportional to the Hg density $\rho(\mathrm{Hg})$.

(b) The Fermi energy E_F was computed to satisfy the relation

$$\int_{-\infty}^{E_F} dE \, N(E) = \int_{-\infty}^{\infty} dE \, N_s(E) \tag{7.3}$$

However, small variations of E_F (± 0.5 eV) were allowed later, during the optimization procedure, to improve the quality of the fittings. This variation of E_F resulted in deviations of less than 5% in the relative areas of the s and the p bands.

(c) The ratio $K/I = 0.11$ was chosen in accordance with the numerical estimate based on Eq. (6.5). This ratio is independent of the composition.

(d) The Hg–Hg coordination number Z was taken from Furukawa's structural model[57] for vacancies (representing the Xe atoms) introduced randomly as a closed-packed lattice. For a fcc lattice the average coordination number is

$$Z = (6\sqrt{2}) \rho(\mathrm{Hg}) a^3 \ , \tag{7.4}$$

yielding a reasonable value $Z = 10$ at $X = 1$.

(e) The parameter A was taken to be proportional to $[\rho(\mathrm{Hg})]^{-1}$, as implied by Eq. (6.1a).

(f) $\sigma(E)$ was calculated from Eq. (6.1) and $\epsilon_2(E) = 4\pi\sigma(E)/\omega$ was subsequently computed over a wide range.

(g) $\epsilon_1(E)$ was calculated from $\epsilon_2(E)$ using the Kramers-Kronig dispersion relation.

(h) The real and imaginary parts of the refractive index n and k were calculated.

(i) The transmittance T_{calc} of a film of thickness d [Eq. (2.4)] was calculated using n and k. The difference between the calculated T_{calc} and the experimental transmittance T_{expt} was minimized for several values of d using the same general curve-fitting procedure as used in Sec. II B for extracting the optical constants of our films. The quality of the fit of the optical data at a given composition is assessed by the mean relative deviation, Δ, of the fitted optical data for N_e energies for each film:

$$\Delta = N_e^{-1} N_f^{-1} \left[\sum_{k=1}^{N_e} \sum_{i=1}^{N_f} \left(\frac{T_{\text{expt}} - T_{\text{calc}}}{T_{\text{expt}}} \right)_{ki}^2 \right]^{1/2} , \qquad (7.5)$$

where N_f denotes the number of films which were simultaneously analyzed.

We have analyzed the dc conductivity and the optical data for the metallic films with $X \leq 0.88$, which correspond to the strong-scattering region. We have attempted a simultaneous fit for the dc conductivity and the optical data for all the conducting Hg-Xe films. In this simultaneous fit of the dc conductivity and the optical data, the dc conductivity is taken as an additional experimental point with a double weight. This simultaneous fit of the dc conductivity and the optical data resulted in the "best fit" $[\sigma(0)]_{\text{calc}}$ of the dc conductivity, as evaluated from Eq. (6.1). This value of $[\sigma(0)]_{\text{calc}}$ was then compared with the experimental value $[\sigma(0)]_{\text{expt}}$. When the relative deviation between $[\sigma(0)]_{\text{calc}}$ and $[\sigma(0)]_{\text{expt}}$ exceeded 100%, we assert that the strong-scattering mechanism for the dc conductivity breaks down. Under these circumstances, only the optical data were utilized to obtain information concerning the density of states of Hg-Xe MRGSM's.

Table I summarizes the relative deviations, Eq. (7.5), which characterize the overall quality of the results of the optimal numerical simulations and which were obtained for Hg-Xe using the model density-of-states functions (7.1) and (7.2). To assess the quality of these fits we would like to mention that the analysis of the experimental data (Sec. II B) in terms of a superposition of Lorentzians [Eq. (2.3)] resulted in relative deviations of $\Delta_e \leq 0.05$. All the values of Δ (Table I) exceed Δ_e, indicating the oversimplified nature of the model densities of states employed by us. Figure 11 displays the concentration dependence of $\sigma(\omega)$ obtained from the best numerical simulations using either GA or SQDE densities of states, which were fitted to the experimental data. We have presented the $\sigma(\omega)$ [or $\epsilon_2(\omega)$] data rather than the $\epsilon_1(\omega)$ data, as the latter quantity in the metallic regime is extremely sensitive to small changes in the optical constants n and k. As it is apparent from Table I the asymmetric SQDE density of states is superior in the high-metal-concentration range $X = 0.88$–0.80, while at the lower metal concentrations $X = 0.76$–0.47 the GA form is superior. This observation concurs with the results of some band-structure calculations for randomly distributed donors[55,56] which indicate that the asymmetric SQDE form might be preferable as a density-of-states model function for high metal concentrations, while the symmetrical form of the Gaussians may prove to be superior for the mixtures with lower metal concentrations. The density of states functions, which provide the best fit of the optical transmittance data are presented in Figs. 12 and 13 for the Gaussian and for the SQDE density of states functions.

Finally, we shall attempt to provide a quantitative analysis of the dc conductivity in the strong-scattering

TABLE I. The quality of the fit for model densities of states to the optical data and the dc conductivity data within the framework of the random-phase model.

Hg atomic fraction X	$[\sigma(0)]_{\text{expt}}$ (sec^{-1})	Δ(%) optical fit	GA[a] $[\sigma(0)]_{\text{calc}}$ (sec^{-1})	$\frac{[\sigma(0)]_{\text{calc}}}{[\sigma(0)]_{\text{expt}}}$	Δ(%) optical fit	SQDE[b] $[\sigma(0)]_{\text{calc}}$ (sec^{-1})	$\frac{[\sigma(0)]_{\text{calc}}}{[\sigma(0)]_{\text{expt}}}$
0.47	· · ·	5.5	1.2×10^{13}	· · ·	12	7×10^{9}	· · ·
0.55	· · ·	8.2	4.4×10^{13}	· · ·	17	7×10^{11}	· · ·
0.66	· · ·	9.1	2.6×10^{14}	· · ·	18	1.2×10^{14}	· · ·
0.73	6×10^{13}	9.1	5.8×10^{14}	9.7	20	4.4×10^{14}	7.1
0.77	2.3×10^{14}	7.8	1.0×10^{15}	4.3	15	8.7×10^{14}	3.8
0.80	9.5×10^{14}	8.4	1.6×10^{15}	1.7	10	1.2×10^{15}	1.26
0.83	2.0×10^{15}	15	2.2×10^{15}	1.1	15	2.4×10^{15}	1.2
0.88	4.4×10^{15}	19	3.5×10^{15}	0.8	13	4.0×10^{15}	0.9

[a]Gaussian model densities of states.

[b]Squared difference of exponents model densities of states.

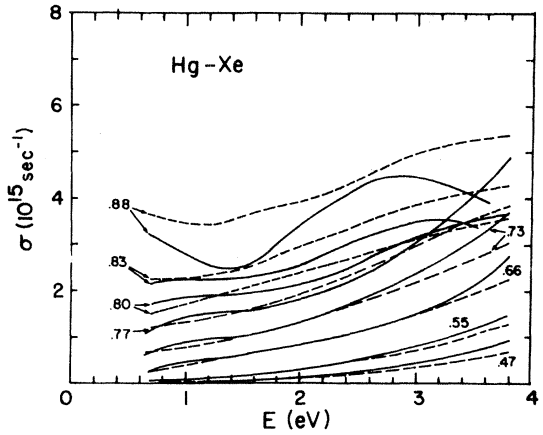

FIG. 11. Optical conductivity $\sigma(E)$ of Hg-Xe mixtures at various Hg concentrations. The number near each curve denotes the mercury atomic fraction. The full lines correspond to the best experimental fit of the optical data with classical-oscillator dielectric functions. The broken lines correspond to the best fit of the optical data with model densities of states. The curves for $X=0.80$, 0.83, and 0.88 represent the results of SQDE model densities-of-states fit. At lower concentrations the results of the fit with Gaussian densities of states are presented.

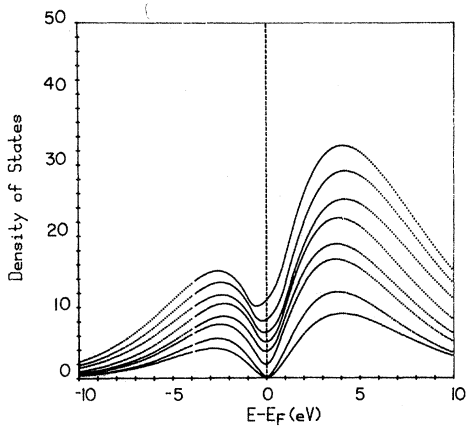

FIG. 13. SQDE (square difference of exponents) model densities of states that provide the best fit for the optical data of Hg-Xe mixtures (subject to the restrictions described in the text). The full lines represent the energy range $E_F-3.8$ eV to $E_F+3.8$ eV, which is directly accessible by our optical spectra. The curves (progressing from those with the highest to the lowest maxima) represent the concentrations $X=0.88$, 0.83, 0.80, 0.77, 0.73, 0.66, 0.55, and 0.47, respectively. Densities of states are in arbitrary units.

metallic regime. We present in Fig. 14 the results of the ratio $[\sigma(0)]_{\text{calc}}/[\sigma(0)]_{\text{expt}}$ as obtained from the simultaneous analysis of dc conductivity and optical data. In the composition range $0.88 \geq X \geq 0.80$ the dc conductivity obtained from the numerical simulations is in good agreement with the experimental data, providing a quantitative confirmation for the proposal that the strong-scattering metallic transport prevails. However, at lower concentrations, the dc conductivity cannot be accounted for in terms of the RPM and the model densities of states that fit the optical data. The fast increase of $[\sigma(0)]_{\text{calc}}/[\sigma(0)]_{\text{expt}}$ with the decrease of metal concentration indicates that the Anderson localization has occurred at the Fermi energy in the pseudogap. The termination of the strong-scattering dc transport at $X=0.80$, as exhibited in Fig. 14, marks the MNMT in the Hg-Xe system.

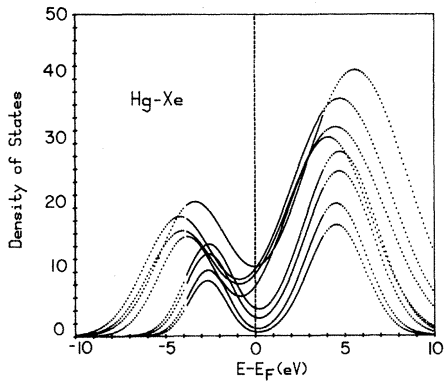

FIG. 12. Gaussian model densities of states that provide the best fit for the optical data of Hg-Xe mixtures (subject to the restrictions described in the text). The full lines represent the energy range $E_F-3.8$ eV to $E_F+3.8$ eV, which is directly accessible by our optical spectra. The curves (progressing from those with the highest to the lowest maxima) represent the concentrations $X=0.88$, 0.83, 0.80, 0.77, 0.73, 0.66, 0.55, and 0.47, respectively. Densities of states are in arbitrary units.

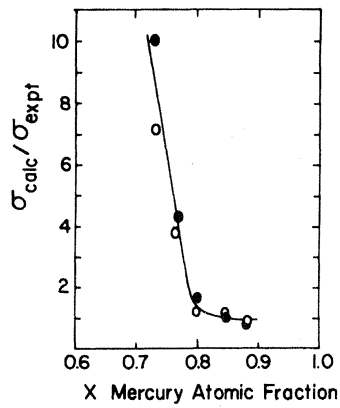

FIG. 14. Ratio of the calculated and the experimental dc conductivity of Hg-Xe mixtures as a function of the Hg atomic fraction X. The calculated values of the dc conductivity were obtained from the simultaneous fit of optical data and dc conductivity to model densities of states within the framework of the random-phase model. The full cycles circles are from the fit of Gaussian densities of states while the open circles are from the SQDE fit.

VIII. CONCLUDING REMARKS

We have explored the optical data and the dc conductivity together with the temperature coefficient of the conductivity (TCC) to provide a complete physical picture for the change in the electronic structure and transport properties of Hg-Xe films over the entire composition range. We felt that the results of the detailed study of the Hg-Xe system will elucidate the general features of a broad class of MRGSM's, which exhibit a continuous change in the transport and optical properties with increasing X. On the basis of our data the following transport regimes can be distinguished in the Hg-Xe system:

(1) Weak-scattering propagation-type metallic regime $X \geq 0.90$. Here $\sigma \geq 5000\ (\Omega\ \text{cm})^{-1}$ and $d\sigma/dT$ is negative.

(2) Strong-scattering diffusive metallic regime $0.90 \geq X \geq 0.80$. Here $5000\ (\Omega\ \text{cm})^{-1} \leq \sigma \leq 600\ (\Omega\ \text{cm})^{-1}$, which can be adequately described, together with $\sigma(\omega)$, by the two-band RPM, while $d\sigma/dT$ is vanishingly small.

(3) The metal-nonmetal transition occurring at $X_M = 0.80 \pm 0.02$. The composition corresponding to the MNMT is obtained from three independent sources: (3a) onset of a positive TCC; (3b) change of the sign of ϵ_1 (at $E = 0.65$ eV); (3c) termination of the strong-scattering metallic transport.

(4) Pseudogap extrinsic transport: In the composition range $0.70 \leq X \leq 0.77$, thermally activated hopping between large-radius localized states prevails even at low temperature.

(5) Intrinsic semiconductor: When $X \leq 0.70$ the optical properties correspond to an amorphous semiconductor.

A central result of the present work is the unambiguous identification of the MNMT and the distinction drawn between the MNMT and the conductivity onset in Hg-Xe MRGSM. It is gratifying that three independent methods provide self-consistent results for X_M, demonstrating the advantage of working with low-temperature amorphous materials in contrast to liquids. In the case of MNMT in two-component liquids, such as metal-ammonia solutions,[58] which are induced by concentration changes, an unambiguous identification of the composition marking the MNMT was not yet accomplished.

We have attempted to account for the electronic structure and transport in Hg-Xe films in terms of physical models appropriate to microscopically homogeneous materials, e.g., strong-scattering metallic transport followed at lower X by a Mott-Anderson MNMT intermediated by thermal hopping. Nevertheless, one should explore further the interrelationship between the topological percolation threshold and the MNMT, following the suggestion of Phelps and Flynn[4,7,59] and others.[12] These workers have attempted to identify the onset of metallic conductivity data for Cs-Xe and for Rb-Kr in terms of the power law[18–24]

$$\sigma \propto (C_a - C_a^*)^p \ , \tag{8.1}$$

with $p = 1.6$–2.0, citing this result as evidence for the applicability of the percolation picture to describe the MNMT in MRGSM's. As the material is microscopically homogeneous, the volume fraction C_a (Fig. 2) has to be utilized to specify the metallic volume fraction. The proposal of Phelps and Flynn[4,7,59] was advanced for monovalent systems, e.g., MRGSM's containing monovalent metals, where electron correlation effects can prevail.[17] This physical picture[4,7,59] is inapplicable for the divalent Hg-Xe system studied herein. The continuous percolation picture predicts that in the concentration range $X = 0.69$–0.77 the dc conductivity for Hg-Xe can be described in terms of Eq. (8.1), with $p = 1.5 \pm 0.1$, the temperature coefficient of σ (TCC) should be small and negative, being roughly equal to the TCC for pure Hg. In contrast, the experimental value of the TCC in that concentration range is large and positive.[10] Thus, our system provides a counterexample against the generality of the proposal of Phelps and Flynn. We believe that the existence of an infinite metallic cluster at the percolation threshold in a microscopically homogeneous MRGSM does not provide a sufficient condition for the onset of metallic conductivity. Consider the MNMT originating from s-p band overlap effects in Hg-Xe. In the infinite cluster just above C_a^* the average Hg-Hg coordination number is low, $Z \simeq 2$–3, as the infinite cluster consists of a superposition of a weakly-bound finite cluster, whereupon the s-p band overlap is not expected to be effective at the topological percolation threshold. This point of view is supported by the results of the recent computer experiments by Srivastava and Weaire,[60] which demonstrate that the Anderson localization in a random binary alloy with nearest-neighbor interactions occurs at a concentration X_M, which is considerably higher than the concentration X^* corresponding to the percolation threshold and that for a three-dimensional network $X_M/X^* \simeq 1.51$. Thus, the MNMT is expected to occur at $X_M = X_A > X^*$, in contrast to the proposal of Phelps and Flynn. We would like to propose that the appearance of an infinite chain of metal atoms at the percolation threshold will result in a dramatic decrease in the activation energy for thermally activated hopping, as the hopping probability between a pair of sites decreases exponentially with the intersite separation. Consequently, the topological percolation threshold marks the onset for effective activated transport, i.e., the conductivity transition in an MRGSM. This proposal is borne out by the experimental dc conductivity data for the Hg-Xe system where the conductivity threshold occurs at $C_a = 0.17$ ($X_C = 0.69$), the value of C_a being close to the continuous percolation threshold[20–24,61] $C_a^* = 0.15$

in a disordered material. The applicability of the power law, Eq. (8.1), for the thermally activated conductivity at $C_a \geq C_a^*$ may be not just accidental but rather reflect enhancement of connectivity between the weakly bound finite clusters when the metal concentration increases just above the percolation threshold.

ACKNOWLEDGMENTS

We wish to thank Gaby Steinberg for his expert assistance in programming. We are grateful to Professor J. C. Thompson for valuable discussions. This research was supported in part by the United States–Israel Binational Science Foundation, Jerusalem, Israel.

APPENDIX: THE RANDOM-PHASE MODEL FOR A TWO-BAND SYSTEM

Let us expand the wave function corresponding to an extended electronic state $|\kappa\rangle$ in terms of a local basis of wave functions $|j,\kappa\rangle$ centered on the sites j occupied by the Hg atoms,

$$|\kappa\rangle = \sum_j a_{j\kappa}|j,\kappa\rangle \tag{A1}$$

and where the local basis states are represented in terms of a superposition of s type, $|s_j\rangle$, and p type, $|p_j\rangle$, states:

$$|j,\kappa\rangle = \alpha_\kappa|s_j\rangle + \beta_\kappa|p_j\rangle \ , \tag{A2}$$

in which α_κ and β_κ correspond to the expansion coefficients of the atomic states s and p in the $|\kappa\rangle$ state. In our analysis we shall represent all the three components of the p state in terms of a single basis function, neglecting the effects of spatial degeneracy and crystal field splitting of the p components. The basic assumption underlying the RPM is that the wave function (A1) on different sites has equal magnitudes, being characterized by complete random phase. As the phases of $a_{j\kappa}$ on different sites are completely random, it will be convenient to reproduce these amplitudes in the form

$$a_{j\kappa} = \exp(i\phi_{j\kappa})/N^{1/2} \ , \tag{A3}$$

where N is the number of Hg atoms in the system, the appearance of $N^{-1/2}$ in Eq. (A3) being implied by the normalization condition for $|\kappa\rangle$. $\phi_{j\kappa}$ is the random phase at site j. We note that only intersite phase relationships are taken to be random, while the coefficients α_κ and β_κ, for given electronic states $|\kappa\rangle$, are taken to be fixed on all the j sites. The normalization condition is $|\alpha_\kappa|^2 + |\beta_\kappa|^2 = 1$, while the s and p character of a given $|\kappa\rangle$ state are $|\alpha_\kappa|^2(|\alpha_\kappa|^2 + |\beta_\kappa|^2)^{-1}$ and $|\beta_\kappa|^2(|\alpha_\kappa|^2 + |\beta_\kappa|^2)^{-1}$, respectively.

The conductivity $\sigma(\omega)$ at the angular frequency ω is expressed in terms of the Kubo-Greenwood formula[62,63]

$$\sigma(\omega) = \frac{B}{\omega}\sum_\kappa\sum_{\kappa'} D_{\kappa\kappa'}(f_{\kappa'} - f_\kappa)\delta(\epsilon_\kappa - \epsilon_{\kappa'} - \hbar\omega) \ , \tag{A4}$$

$$B = \pi e^2/m^2\Omega \ , \tag{A4a}$$

$$D_{\kappa\kappa'} = |\langle\kappa|\hat{p}|\kappa'\rangle|^2 \ , \tag{A4b}$$

where Ω is the volume of the system, $D_{\kappa\kappa'}$ is the transition operator expressed in terms of the matrix element of the momentum operator $\hat{p}$ between the states $|\kappa\rangle$ and $|\kappa'\rangle$ of energies ϵ_κ and $\epsilon_{\kappa'}$, whose occupation probabilities are f_κ and $f_{\kappa'}$.

We now proceed to the calculation of the transition operator invoking the RPM.[48] According to the RPM[49,50] Eq. (A4b) can be replaced by its configurational average, which is expressed in the form

$$\langle D_{\kappa\kappa'}\rangle_c = N^{-1}\sum_{j'}|\langle j\kappa|\hat{p}|j',\kappa'\rangle|^2 \ , \tag{A5}$$

where $\langle\ \rangle_c$ denotes the configurational average. We shall further advance the reasonable assumption that the only nonvanishing contributions to Eq. (A5) originate from diagonal one-center intrasite contributions with $j = j'$, and from the two-center interstate contributions from neighboring Hg sites with j and j' corresponding to nearest neighbors. The transition operator is

$$\langle D_{\kappa\kappa'}\rangle_c = N^{-1}|\langle j,\kappa|\hat{p}|j,\kappa'\rangle|^2 + N^{-1}Z|\langle j,\kappa|\hat{p}|j',\kappa'\rangle|^2 \ , \tag{A6}$$

where Z is the coordination number of Hg atoms, which depends on N. The one-center contribution to Eq. (A6) was obtained in the form

$$|\langle j,\kappa|\hat{p}|j,\kappa'\rangle|^2 = (\alpha_\kappa\beta_{\kappa'} - \beta_\kappa\alpha_{\kappa'})^2 I \ , \tag{A7}$$

$$I = |\langle s_j|\hat{p}|p_j\rangle|^2 \tag{A8}$$

where, for the sake of simplicity, the expansion coefficients α_κ and β_κ were taken to be real. The two-center contribution to Eq. (6.6) is

$$|\langle j,\kappa|\hat{p}|j',\kappa'\rangle|^2 = |\alpha_\kappa\alpha_{\kappa'}\langle s_j|\hat{p}|s_{j'}\rangle + \beta_\kappa\beta_{\kappa'}\langle p_j|\hat{p}|p_{j'}\rangle + \alpha_\kappa\beta_{\kappa'}\langle s_j|\hat{p}|p_{j'}\rangle + \beta_\kappa\alpha_{\kappa'}\langle p_j|\hat{p}|s_{j'}\rangle|^2 \ , \tag{A9}$$

where j and j' are nearest neighbors. In view of our current ignorance of the numerical values of the intersite integrals appearing in Eq. (A9), we shall take

all these integrals to be equal and define

$$K \cong |\langle s_j|\hat{p}|s_{j'}\rangle|^2 \cong |\langle p_j|\hat{p}|p_{j'}\rangle|^2 \cong |\langle s_j|\hat{p}|p_{j'}\rangle|^2 \ . \tag{A10}$$

The two-center contribution to Eq. (A16) now assumes the form

$$|\langle j,\kappa|\hat{p}|j',\kappa'\rangle|^2 = K(1+2\alpha_{\kappa'}\beta_{\kappa'}+2\alpha_\kappa\beta_\kappa+4\alpha_\kappa\beta_{\kappa'}\alpha_{\kappa'}\beta_\kappa) \ . \tag{A11}$$

Armed with Eqs. (A6), (A7), and (A11), the transition operator takes the form

$$D_{\kappa\kappa'} = N^{-1}I(\alpha_\kappa^2\beta_{\kappa'}^2\beta_{\kappa'}^2+\beta_\kappa^2\alpha_{\kappa'}^2-2\alpha_\kappa\alpha_{\kappa'}\beta_\kappa\beta_{\kappa'}) + N^{-1}ZK(1+2\alpha_{\kappa'}\beta_{\kappa'}+2\alpha_\kappa\beta_\kappa+4\alpha_\kappa\beta_{\kappa'}\alpha_{\kappa'}\beta_\kappa) \ . \tag{A12}$$

It will be convenient at this stage to define the s and p densities of states in terms of the s and p character,

$$N_s(E) = \Omega^{-1}\sum_\kappa \alpha_\kappa^2\delta(E-E_\kappa) \ , \tag{A13a}$$

$$N_p(E) = \Omega^{-1}\sum_\kappa \beta_\kappa^2\delta(E-E_\kappa) \ , \tag{A13b}$$

so that the total density of states, $N(E)$,

$$N(E) = \Omega^{-1}\sum_\kappa \delta(E-E_\kappa) \tag{A14}$$

can be expressed as the superposition

$$N(E) = N_s(E)+N_p(E) \ . \tag{A15}$$

Finally, we shall define the hybrid density of states,

$$N_{sp}(E) = \Omega^{-1}\sum_\kappa \alpha_\kappa\beta_\kappa\delta(E-E_\kappa) \ , \tag{A16}$$

which will be approximated in terms of the relation

$$N_{sp}(E) = [N_s(E)N_p(E)]^{1/2} \ . \tag{A17}$$

We are now able to express the optical conductivity, Eq. (A4), at $T=0$ with the aid of Eq. (A12) and the definition, Eqs. (A13)–(A17), which lead to Eq. (6.1).

[1] R. C. Cate, J. G. Wright, and N. E. Cusack, Phys. Lett. 32A, 467 (1970).
[2] H. Endo, A. I. Eatah, J. G. Wright, and N. E. Cusack, J. Phys. Soc. Jpn. 34, 666 (1973).
[3] A. I. Eatah, N. E. Cusack, and J. G. Wright, Phys. Lett. 51A, 149 (1975).
[4] D. J. Phelps, R. Acvi, and C. P. Flynn, Phys. Rev. Lett. 34, 23 (1975).
[5] Z. Shanfield, P. A. Montano, and P. H. Barrett, Phys. Rev. Lett. 35, 1789 (1975).
[6] O. Hunderi and R. Ryberg, Phys. Lett. 51A, 167 (1975).
[7] D. J. Phelps and C. P. Flynn, Phys. Rev. B 14, 5279 (1976).
[8] G. Hilder and N. F. Cusack, Phys. Lett. 62A, 163 (1977).
[9] R. Ryberg and O. Hunderi, J. Phys. C 10, 3559 (1977).
[10] O. Cheshnovsky, U. Even, and J. Jortner, Solid State Commun. 22, 745 (1977).
[11] N. A. McNeal and A. M. Goldman, Phys. Lett. 61A, 268 (1977).
[12] K. Epstein, E. D. Dahlberg, and A. M. Goldman, Phys. Rev. Lett. 43, 1889 (1979).
[13] B. Raz, A. Gedanken, U. Even, and J. Jortner, Phys. Rev. Lett. 28, 1643 (1972).
[14] O. Cheshnovsky, U. Even, and J. Jortner, Phys. Lett. 71A, 255 (1979).
[15] R. Danor, O. Cheshnovsky, U. Even, and J. Jortner, Philos. Mag. B 39, 99 (1979).
[16] J. J. Quinn and J. G. Wright, in *Liquid Metals—1976,* IOP Conf. Ser. No. 30 (IOP, Bristol and London, 1977), p. 430.
[17] (a) N. F. Mott, *Metal-Insulator Transition* (Taylor and Francis, London, 1974). (b) *The Metal–non-Metal Transition in Disordered Systems,* edited by L. R. Friedman and D. P. Tunstall (SUSSP Publication, Edinburgh, 1978).
[18] R. Kubo, J. Phys. Soc. Jpn. 17, 975 (1962).
[19] S. Kirkpatrick, Phys. Rev. 27, 1722 (1971).
[20] K. S. Shante and S. Kirkpatrick, Adv. Phys. 20, 325 (1971).
[21] I. Webman, J. Jortner, and M. H. Cohen, Phys. Rev. B 11, 2885 (1975).
[22] I. Webman, J. Jortner, and M. H. Cohen, Phys. Rev. B 13, 713 (1976).
[23] I. Webman, J. Jortner, and M. H. Cohen, Phys. Rev. B 14, 4737 (1976).
[24] I. Webman, J. Jortner, and M. H. Cohen, Phys. Rev. B 15, 5712 (1977).
[25] B. Abeles, Ping Sheng, M. D. Coutts, and Y. Arie, Adv. Phys. 24, 407 (1975).
[26] O. Cheshnovsky, Ph.D. thesis (Tel-Aviv University, 1979) (unpublished).
[27] I. H. Malitson, F. V. Murphy, Jr., and W. S. Rodney, J. Opt. Soc. Am. 48, 72 (1958).
[28] H. W. Verleur, J. Opt. Soc. Am. 58, 1356 (1968).
[29] F. James and M. Ross, Comput. Phys. Commun. 10, 343 (1975).
[30] H. Mayer, *Physik dünner Schichten* (Wissenschaftliche Verlagsgesellschaft MbH., Stuttgart, 1950), Teil I, p. 207. See also P. O. Nilsson, Appl. Opt. 7, 435 (1968).
[31] F. Wooten, *Optical Properties of Solids* (Academic, New York, 1972).
[32] N. W. Ashcroft and J. Lekner, Phys. Rev. 145, 83 (1966).
[33] (a) G. L. Pollack, Rev. Mod. Phys. 36, 748 (1964). (b) W. Schulze and D. H. Kolb, Chem. Soc. Faraday Trans. II 70, 1098 (1974).
[34] G. Schönherr, Dissertation (Philipps-Universität, Marburg/Lann) (unpublished).
[35] W. J. Choyke, S. H. Vosko, and T. W. O'Keefe, Solid

State Commun. 9, 361 (1971).
[36]H. Bülow and W. Buckel, Z. Phys. 145, 141 (1956).
[37]R. W. Cohen, G. D. Cody, M. D. Coutts, and B. Abeles, Phys. Rev. B 8, 3689 (1973).
[38]J. I. Gittleman and B. Abeles, Phys. Rev. B 15, 3273 (1977).
[39]F. A. Meier, Ph.D. thesis, (Catholic University of Nijmegen, 1973) (unpublished).
[40]J. C. Maxwell-Garnett, Philos. Trans. R. Soc. London 203, 385 (1904); 205, 237 (1906).
[41]L. D. Landau, E. M. Lifshitz, *Electrodynamics of Continuous Media* (Pergamon, Oxford, 1960), p. 261.
[42]M. Capizzi, G. A. Thomas, F. De Rosa, R. N. Bhatt, and T. M. Rice, Phys. Rev. Lett. 44, 1019 (1980).
[43]N. F. Mott and E. A. Davis, *Electronic Processes in Noncrystalline Materials* (Clarendon, Oxford, 1971 and 1979).
[44]O. Cheshnovsky, U. Even, and J. Jortner, Philos. Mag. B 44, 1 (1981).
[45]F. Yonezawa, Y. Ishida, F. Martino, and S. Asano, in *Liquid Metals—1976,* IOP Conf. Ser. No. 30 (IOP, Bristol and London, 1977).
[46]N. F. Mott, Philos. Mag. 31, 217 (1975).
[47]M. H. Cohen, in *Proceedings of the Symposium on Semiconductor Effects of Amorphous Solids* (North-Holland, Amsterdam, 1970).
[48]N. F. Mott, Adv. Phys. 16, 49 (1967).
[49]N. K. Hindley, J. Non-Cryst. Solids 5, 17 (1970).
[50]L. Friedman, J. Non-Cryst. Solids 6, 329 (1971).
[51]U. Even and J. Jortner, Philos. Mag. 25, 715 (1972).
[52]K. Maschke and P. Thomas, Phys. Status Solidi B 41, 743 (1970).
[53]W. Paul, G. A. M. Connell, and R. J. Temkin, Adv. Phys. 22, 531 (1973).
[54]T. Holstein and L. Friedman, Phys. Rev. 165, 1019 (1968).
[55]F. Cyrot-Lackmann and J. P. Gaspard, J. Phys. C 7, 1829 (1974).
[56]H. Aoki and H. Kamimura, J. Phys. Soc. Jpn. 40, 6 (1976).
[57]K. Furukawa, Sci. Rep. Res. Inst. Tohoku Univ. A12, 368 (1960).
[58]J. C. Thompson, *Electrons in Liquid Ammonia* (Clarendon, Oxford, 1976).
[59]D. J. Phelps and C. P. Flynn, Phys. Rev. B 14, 5279 (1976).
[60]V. Srivastava and D. Weaire, Phys. Rev. B 18, 6635 (1978).
[61]H. Scher and R. Zallen, J. Chem. Phys. 53, 3959 (1970).
[62]R. Kubo, Can. J. Phys. 34, 1274 (1956).
[63]D. A. Greenwood, Proc. Phys. Soc. London Sect. A 71, 585 (1958).